analytical chemistry

Article

Cite This: *Anal. Chem.* 2019, 91, 13658−13664

pubs.acs.org/ac

Variable-Angle Nanoplasmonic Fluorescence Microscopy: An Axially Resolved Method for Tracking the Endocytic Pathway

Min Chen, Xiao-Hui Pan, Qian Liu, Si-Xin Huo, Shuo-Hui Cao, Yan-Yun Zhai, Yan Zhao, and Yao-Qun Li*

Department of Chemistry and the MOE Key Laboratory of Spectrochemical Analysis & Instrumentation, College of Chemistry and Chemical Engineering, Xiamen University, Xiamen 361005, P.R. China

Supporting Information

ABSTRACT: The study of endocytosis, which encompasses diverse mechanisms in biology, requires the utilization of high axial resolution to monitor molecular behavior on both the cell surface and interior of the cell. We have designed a novel axially resolved fluorescence microscopic technique, termed variable-angle nanoplasmonic fluorescence microscopy. The proof-of-principle of this approach is achieved by selectively following the events in the vicinity of a cell membrane or in a cell. We use a 30 nm Au-coated semitransparent coverslip as the nanoplasmonic chip to achieve both surface plasmon resonance excitation and critical angle excitation by tuning the incident angles. This approach leads to improved axial resolution compared to total internal reflection fluorescence microscopy, which is a common imaging technique in cell biology. It offers a unique opportunity to semiquantitatively determine fluorophore axial distributions in the cell. Observing the epidermal growth factor receptor-mediated endocytosis in Caski cells clearly demonstrates the potential application of this new method for cell biology studies.

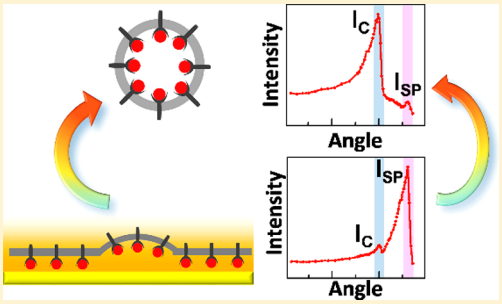

Endocytosis regulates the uptake of nutrients and signal transduction between intracellular milieu and the extracellular environment. During this process, cells internalize macromolecules and particles derived from the plasma membrane into transport vesicles. Monitoring the endocytic pathway in situ is essential for understanding cellular activities, such as cell growth, proliferation, differentiation, and apoptosis.[1−5] High axial resolution is required to trace the cargo and receptors from the cell membrane to the cytoplasm during endocytosis. Fluorescence microscopy is a popular optical method in cell biology, as it displays both high sensitivity and specificity.[6−10] Various fluorescence microscopic techniques have been proposed for promoting lateral resolution beyond the light diffraction limit, resulting super-resolution imaging of fine structures.[11−14] On the other hand, a dramatic improvement is still needed for high axial resolution, which is even more affected by diffraction.[15]

One of the most prevalent imaging techniques that has been employed in endocytosis is total internal reflection fluorescence microscopy (TIRFM), which is used for recording the biological activities on or near the cell surface because of its advantageous evanescent field excitation within 100−200 nm.[16−21] However, molecular events deep inside the cells are difficult to visualize due to the limited evanescent field depth. This limitation can be overcome by utilizing a large incident angle that is still slightly smaller than the critical angle. As the excitation beam could refract into the sample medium with a large angle, the detection depth is extended while background signals are minimized. This variable-angle epifluorescence microscopy,[22] also named as pseudo- or quasi-TIRFM[23,24] and highly inclined and laminated optical sheet,[25] can image molecular dynamics in deeper areas of cells.

Surface plasmon coupled emission microscopy (SPCEM), basing upon the strong interaction of surface plasmons with the excited fluorophores in the near-field, is an alternative to TIRFM for near-field imaging.[26−29] The evanescent excitation and distance-dependent emission coupling of SPCEM could limit the imaging depth to 40−70 nm.[26,30] Studies have shown that SPCEM possesses higher imaging contrast and background suppression capability in near-field detection compared with TIRFM. Such advantages have allowed SPCEM to be applied in protein detection,[31−33] plasma membrane imaging[29,34,35] and muscle fiber imaging.[36−38] This technique thus provides an opportunity to develop an imaging method with higher axial resolution.

In this report, we propose an approach named variable-angle nanoplasmonic fluorescence microscopy (VANFM) for subcellular imaging with high resolution in the axial direction by taking advantage of the relationship between the fluorophore-substrate distance and incident angles. A 30 nm semitransparent Au substrate is selected to obtain surface plasmon resonance (SPR) excitation and critical angle excitation on the same chip. It thus expands the imaging depth from the close vicinity to far-field so that we can

Received: June 23, 2019
Accepted: October 2, 2019
Published: October 2, 2019

DOI: 10.1021/acs.analchem.9b02845
Anal. Chem. 2019, 91, 13658−13664

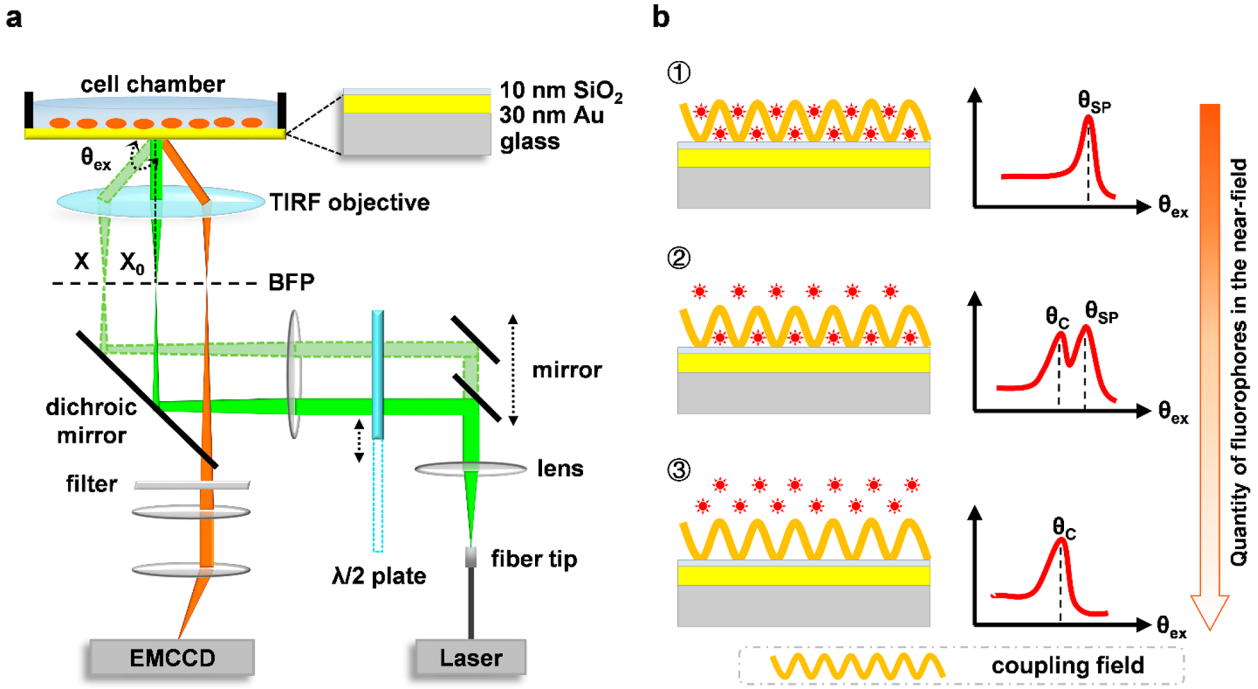

Figure 1. Schematic of VANFM. (a) The VANFM setup. VANFM is comprised of a commercial TIRFM, equipped with a half wave plate ($\lambda/2$ plate) in the incident pathway to adjust the excitation polarization. The incident angle can be precisely tuned by adjusting the mirror position. For imaging, the coverslip is sequentially coated with 30 nm Au and 10 nm SiO_2. (b) The relationship between the fluorophore-locations and angle-distributions is as follows: ① when the fluorophores are located in the near-field, there is only one angular peak at θ_{SP}; ② when the fluorophores are located in both the near-field and far-field, there are two peaks at θ_C and θ_{SP}, respectively, and the peak intensity is positively related to the component quantity in each region; and ③ when the fluorophores are in the far-field, only one peak at θ_C appears, and the angular distribution curves can be obtained by incident-angle scanning.

visualize both the cell surface and interior with ultrahigh axial-resolution for the membrane. In this method, we utilize angular distribution curves and peak intensity ratios to semi-quantitatively estimate the axial distributions of fluorophores in subcellular regions. This effectively overcomes the interference of the fluctuations in the excitation intensity, fluorophore concentration, and individual differences among cells in intensity-based fluorescence microscopy. By observing the endocytosis of Caski cells mediated by the epidermal growth factor receptor (EGFR), we found that the angular distribution curves and signal peak intensity ratios changed regularly with the endocytic pathway. VANFM yields both higher resolution and better fluorophore positioning capability than TIRFM in the axial dimension.

EXPERIMENTAL SECTION

Materials. Rhodamine B (RhB; Sigma-Aldrich, U.S.A.), poly(methyl methacrylate) (PMMA, MW: 350 000; Alfa, U.S.A.), anisole (Sigma-Aldrich), propidium iodide (PI, Sigma-Aldrich, U.S.A.), and 1,1′-dioctadecyl-3,3,3′,3′-tetramethylindocarbocyanine perchlorate (DiI; Sigma-Aldrich, U.S.A.) were utilized. Ethyl alcohol, H_2SO_4, H_2O_2, NaCl, KCl, $Na_2HPO_4{\cdot}12H_2O$, and KH_2PO_4 were all analytical grade reagents (all from the Sinopharm Chemical Reagent Co., Ltd. Shanghai, China). Ultrapure water was prepared using a Milli-Q system.

Preparation of Metallic Substrates. Metallic substrates were prepared by depositing 2 nm Cr/30 nm Au/10 nm SiO_2 on a coverslip (FIS12-545-102; Fisherbrand) in sequence with magnetron sputtering. Before incubation with cells, all slides were washed with ultrapure water and immersed in EtOH for 3 h, followed by exposure to UV light for approximately 15 min and washing twice with 10 mM PBS buffer.

Variable-Angle Nanoplasmonic Fluorescence Microscope. Fluorescence images were obtained via a microscope built on top of commercial total internal reflection fluorescence microscope (Ti−U; Nikon). The experimental setup is illustrated in Figure 1a, which was equipped with a 561 nm laser system (Coherent), a TIRF filter cube (TRF 49909, Chroma), an APO TIRF objective (100 ×, NA = 1.49, Nikon), and an electron multiplying charge coupled device (EMCCD) camera (iXon Ultra 897, Andor). A $\lambda/2$ plate was inserted in the incident light pathway to adjust the excitation polarization from s-pol to p-pol. The laser is highly polarized after passing through the optical elements (section 1, Supporting Information). The incident angle could be precisely tuned in the range of 0° (epifluorescence illumination, EPI) to 80° by controlling the mirror position with NIS-Elements AR (Nikon) software (see details in section 2, Supporting Information).

Angular Distribution Curve and Relative Ratio. In order to obtain the angular distribution curves of the fluorescence, images were taken at intervals of ∼4° in the range of 0−45° and ∼1° in the range of 45−80° (the exact step depends on $|X-X_0|$, please see section 2, Supporting Information). The angle-scanning process was controlled using NIS-Elements AR (Nikon) software and took about 2 min. Then the critical angle and the SP angle were determined from the two peak maxima in the angular distribution curve. The critical angle and the SP angle remains the same for different cellular samples when using identical nanoplasmonic chips. Therefore, for any subject, only two images were

DOI: 10.1021/acs.analchem.9b02845
Anal. Chem. 2019, 91, 13658−13664

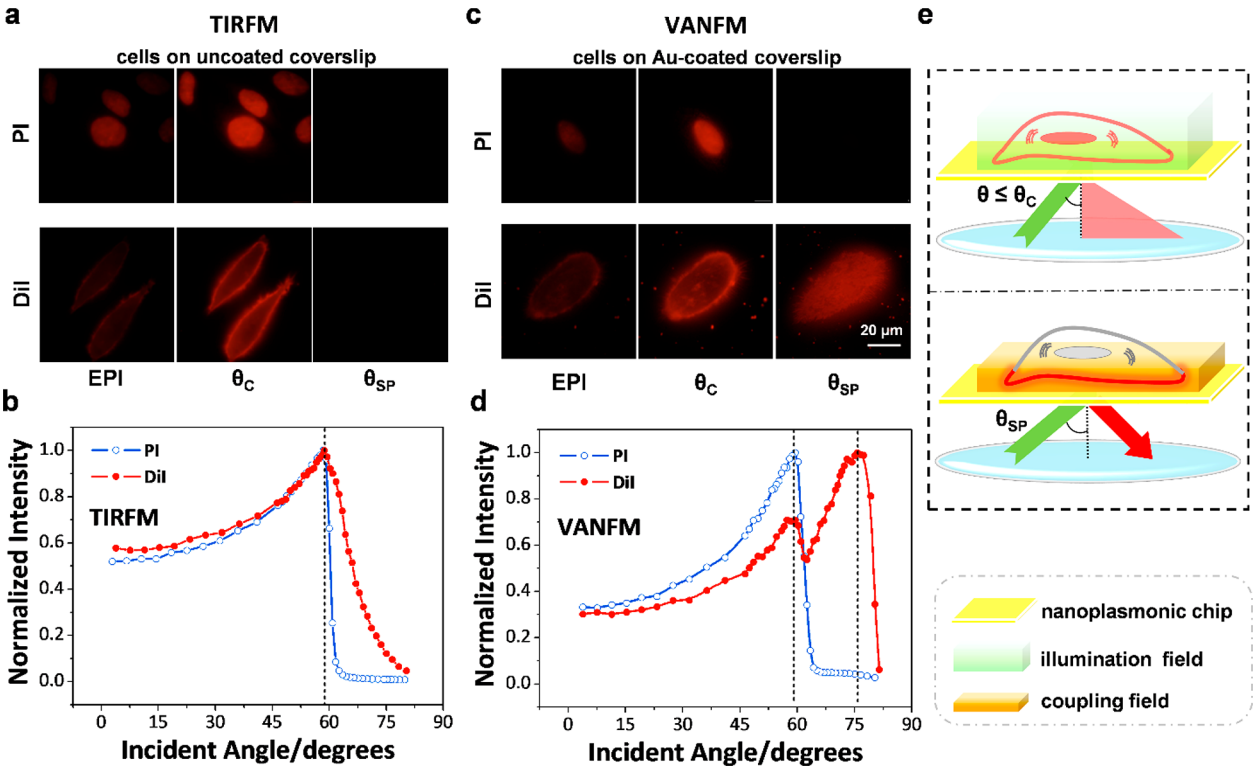

Figure 2. Subcellular imaging with TIRFM and VANFM. (a and c) Fluorescence images and (b and d) normalized fluorescence intensity as a function of the incident angle of cells (a and b) cultured on an uncoated coverslip (TIRFM) and (c and d) on a Au-coated coverslip (VANFM). The nuclei and membranes of cells were dyed with PI and DiI, respectively. For nucleus-labeled cells, the bright region of the nucleus was chosen as the region of interest (ROI). Upon staining with membrane dyes, the image of the cell at θ_C appears as a dim area surrounded by a higher circle, corresponding to an accumulation of dye in the high curvature membrane at the boundary of the cell-chip contact. Therefore, only the dim area corresponding to the flat membrane at the chip contact was taken into account for analysis (scale bar: 20 μm). (e) Schematic of different excitation modes on the Au-coated coverslip.

required to obtain the relative I_{SP}/I_C ratio, thus providing a semiquantitative estimate of the axial location of the fluorophores. The experimental time for taking two images is only 1−2 s, offering significant advantage for the study of living cell. Afterward, the region of interest (ROI) of images were analyzed by NIS-Elements AR Analysis.

Cell Culture and Labeling. Caski cells, purchased from the Cell Bank of the Chinese Academy of Sciences in Shanghai, were cultured in Dulbecco's modified Eagle's medium (DMEM, HyClone) supplemented with 10% fetal bovine serum (Hyclone) at 37 °C under 5% CO_2. After digestion by trypsin, cells in the logarithmic phase were incubated with the cleaned substrates overnight. The labeling process for DiI was as follows: cells were washed three times with PBS and labeled in 10 mmol/L DiI/PBS solution for 20 min at room temperature. Then, the cells were washed three times with PBS buffer and fixed with a 4% paraformaldehyde (PFA) solution. The PFA/PBS solution was washed off by PBS before measurement. To label the nucleus, cells were first fixed with 70% EtOH at −20 °C overnight and then washed three times with PBS. The cells were labeled in 40 mmol/L PI/PBS solution for 2 h and washed three times with PBS.

EGFR-Mediated Endocytosis. Caski cells were seeded on the cleaned substrates overnight. To follow the fate of EGFR and its ligand EGF over time, we first incubated cells with Alexa Fluor 555 conjugated to EGF (AF 555-EGF) on ice at 4 °C for 1 h, a temperature that allows for receptor−ligand binding but prevents their internalization.[6,39,40] Cells were shifted to 37 °C, after washing the probes off, to recover the internalization of receptor−ligand complexes by the endosome located deeper within cells. Cells were fixed with 4% PFA after recovery for different periods of time (0, 5, 10, and 30 min, respectively), followed by imaging with VANFM.

RESULTS AND DISCUSSION

Schematic of VANFM. In TIRFM, when the excitation light enters a sample from a high refractive index glass substrate, reflection and refraction occur at the interface. When the incident angle is above the critical angle (θ_C), the incident light is totally reflected while its energy penetrates into the sample to produce an evanescent field.[39,41] Evanescent field intensity in the sample decays exponentially in the z-dimension, whose penetration depth decreases with increasing θ (see equation in section 3, Supporting Information). At the incident angle of θ_C, both evanescent field excitation and refractive field excitation exist (defined as critical angle excitation). In this case, as the evanescent field intensity is greater than the incident light intensity, an enhanced fluorescence signal can be obtained.[41] As the angle continues to increase, the evanescent field intensity decays exponentially, and the fluorescence signal rapidly diminishes. Thus, the fluorescence signal reaches a peak value at θ_C.

For metal-coated glass, when the polarization-matched excitation light is incident at an angle satisfying the resonance condition (θ_{SP}, $\theta_{SP} > \theta_C$), the fluorophores located in the near-field range of the metal film can be selectively excited by the evanescent field (defined as SPR excitation). The excited fluorophores can be coupled with surface plasmons to produce

DOI: 10.1021/acs.analchem.9b02845
Anal. Chem. 2019, 91, 13658−13664

an enhanced fluorescence signal.[42−46] This surface plasmon-coupled emission (SPCE) is distance-dependent.[31,47−50] Studies have shown that the detection volume of SPCEM is limited by two near-field factors: one is the depth of the evanescent wave and the other is the coupling distance of surface plasmons. As a consequence, the effective detection depth of SPCEM is approximately 50 nm in the near-field (section 3, Supporting Information).[26,30,51] Thus, the fluorophores can be coupled to surface plasmons only if the fluorophore-substrate distance is less than the coupling distance of the SPCE. When the distance goes beyond the SPCE coupling range, the intensified signal at θ_{SP} disappears. VANFM can therefore provide a confined axial-section with the thickness of around 50 nm with SPR excitation, which is advantageous over conventional TIRFM.

Based on the above properties, we designed a VANFM system based on a semitransparent metal substrate. The setup of VANFM was developed based on a commercial TIRFM (Nikon Ti) with a Kretschmann (KR) configuration, with which we can regulate the incident angle and polarization of the excitation precisely (Figure 1a, see details in the Experimental Section). The only additional device for the VANFM system, when compared with conventional TIRFM, is a half wave plate ($\lambda/2$ plate) in the excitation pathway to adjust the polarization. We applied VANFM to scan the fluorescent nanofilm and the results showed the same polarization and angular distribution as calculated simulation with Fresnel equation (section 4, Supporting Information). This demonstrated the excellent capability of VANFM in SPCE imaging.

A 30 nm Au-coated substrate allows the nanoplasmonic chip to meet the SPCE coupling while transmitting part of the incident light. The critical angle excitation of the glass substrate or the SPR excitation of the metal substrate is achieved on the same substrate by adjusting the incident excitation angle. When the incident angle reaches θ_C, the far-field fluorophore is excited by the critical angle excitation mode in the range of several hundred nanometers. When the incident angle approaches θ_{SP}, it turns into SPR excitation, acting only with the near-field fluorophore in the coupling range. Therefore, in VANFM, the angular dependence of the fluorescence intensity varies with the fluorophore-substrate distance (Figure 1b). When fluorophores are located in different regions, the excitation modes of the near-field component and the far-field component may be different. The signals of these two do not interfere and only reflect the distribution of fluorophores at a given distance range. Changing the incident angle can thus selectively enhance the fluorescence of the near-field or far-field. Therefore, we can detect different subcellular regions by changing the incident angle. At the same time, comparing the relative ratio of the near-field component signal (I_{SP}) to the far-field component signal (I_C) opens up a new opportunity to semiquantitatively determine the axial motion of molecules in the cell.

Subcellular Imaging with TIRFM and VANFM. First, we examined the abilities of traditional TIRFM and VANFM for subcellular imaging. Caski cells grew into a monolayer after culturing overnight on the uncoated and 30 nm Au-coated coverslip. The nucleus and membrane were then stained with 1,1′-dioctadecyl-3,3,3′,3′-tetramethylindocarbocyanine perchlorate (DiI) and propidium iodide (PI), respectively, both of which emit red fluorescence under 561 nm excitation. For adherent cells, PI is located in the nuclear region of a few hundred nanometers from the substrate, while DiI is mainly distributed in the cell membrane region, whose distance from the substrate is closer. Figure 2 shows the changes in the fluorescence images and intensities of cells for different incident angles. The experiments showed little difference in the angular distributions between membrane-stained and nucleus-stained cells on the glass substrate (Figure 2a,b). As the incident angle increased, the signal became the strongest at θ_C and then decayed rapidly. There is only one angular peak at θ_C in the angular distribution curve, which is consistent with the change in the excitation intensity for different incident angles reported in the literature.[41] It can be seen that the angular distribution in the conventional TIRFM does not change with the fluorophore-interface distance as there is no induction of surface plasmons. Therefore, it is impossible to distinguish different subcellular regions by angle scanning with TIRFM.

For cells on the Au-coated coverslip, there were significant differences in the angular distribution and polarization. We found that only p-polarized light can effectively excite enhanced fluorescence images (section 5, Supporting Information), which confirms the p-polarized property.[32,52,53] Furthermore, the PI and DiI signals exhibited different angular distributions as the incident angle changed (Figure 2c,d). For nucleus-labeled samples, the location of the fluorophores is out of the SPCE coupling range, and thus the fluorophores could not be coupled to surface plasmons. Therefore, the angular distribution of PI signals was similar to that of the glass coverslip (Figure 2d, blue curve). Only one angular peak was generated at θ_C, resulting from the enhancement of the total internal reflection evanescent field. As the incident angle increased, the signal dropped rapidly. However, for membrane-labeled samples, the fluorophores in the basal cell membrane are mainly distributed in the near-field within the SPCE coupling range. As a consequence, DiI could interact with surface plasmons to generate an enhanced signal at θ_{SP} (Figure 2d, red curve). The intensity was approximately 3 times stronger than that observed in the EPI mode. As we can see from the curve, there was still a peak at θ_C, which is supposed to be the contribution of the membrane-bound organelles in the cell.

As the incident angle increased, the imaging plane gradually moved to the vicinity of the interface (Figure 2c). When the excitation was incident at θ_C, an intensified nucleus structure can be observed, indicating that the imaging depth can penetrate into the far-field. Increasing the incident angle to θ_{SP} led to the disappearance of the nucleus structure but highlighted the membrane structure, which proves that the imaging depth is limited within the near-field. Such variation of imaging depth with different incident angles is caused by the change in the excitation mechanism (Figure 2e). When the incident angle is smaller than θ_C, samples are illuminated by refracted light, which could pass through the bulk solution to excite distal fluorophores, even in the inner part of the cell. As the incident angle approaches θ_C, the incident light undergoes total internal reflection, producing an evanescent wave that decays exponentially with the distance. Given that the penetration depth of the evanescent field becomes shallower as the incident angle increased, only molecules within or near the basal membrane could be illuminated. Meanwhile, due to the coupling distance limitation, the SPCE detection volume is even smaller than TIRF.[26,29,30] This fact further reduces the far-field background from the cell contents or culture medium, improving the resolution and contrast of near-field imaging.

DOI: 10.1021/acs.analchem.9b02845
Anal. Chem. 2019, 91, 13658−13664

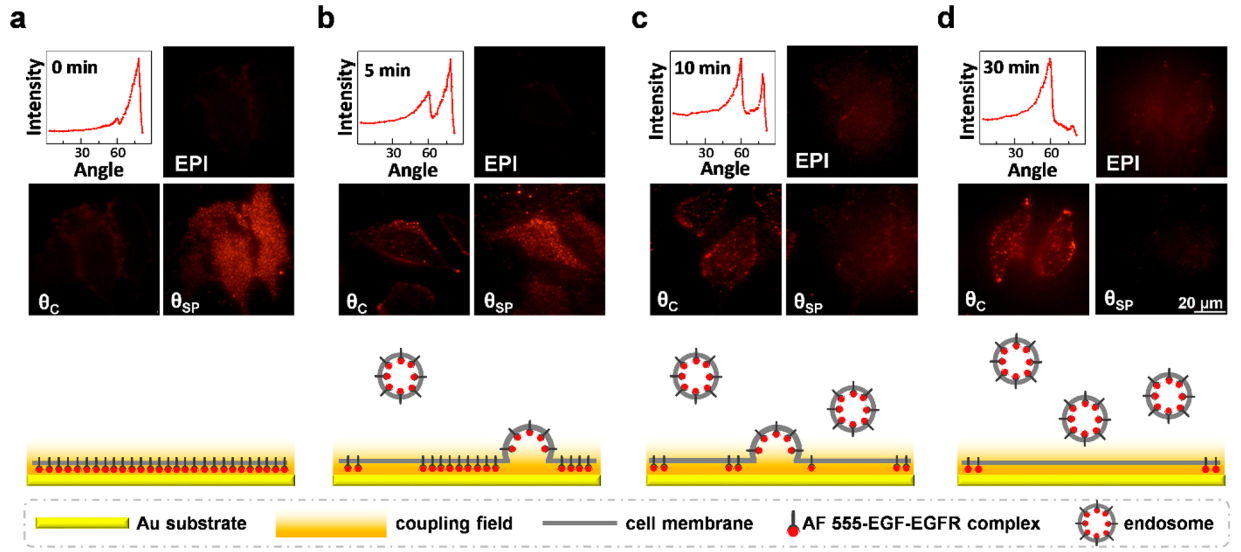

Figure 3. VANFM imaging for EGFR-mediate endocytosis. (a–d) Angle-dependent fluorescence intensity, fluorescence images, and schematics of the ligand–receptor complex distributions after recovery at room temperature for (a) 0, (b) 5, (c) 10, and (d) 30 min, respectively (scale bars: 20 μm).

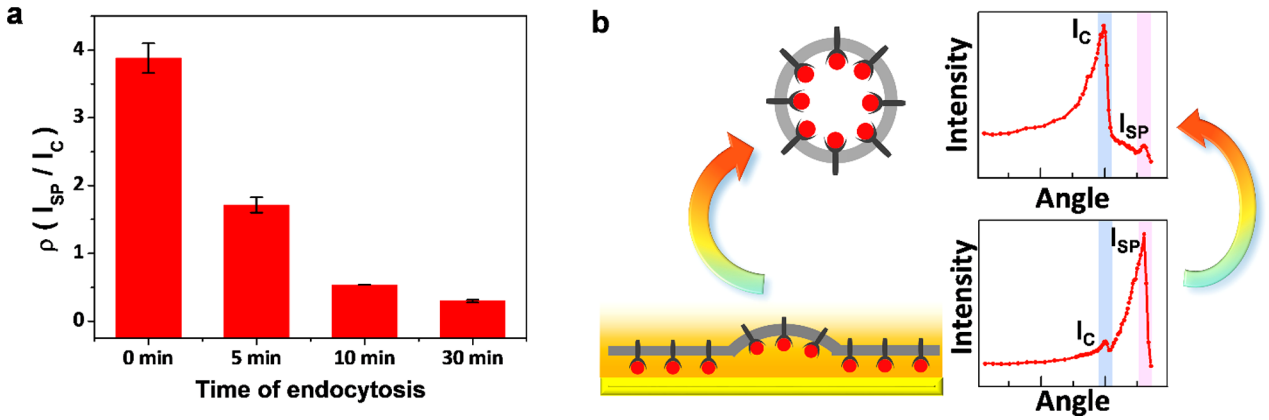

Figure 4. Evaluation of the endocytic pathway. (a) Calculated relative ratio (ρ) of the near-field component signal (I_{SP}) to the far-field component signal (I_C) over time in the EGFR-mediated endocytosis ($\rho = I_{SP}/I_C$). Each value is the average result of three cells on the same nanoplasmonic chip (N = 3). (b) Schematic of the variation tendency of angle-dependent fluorescence along with the internalization of ligand–receptor complexes.

Given the above, we can conclude that the far-field fluorescence inside the cell is mainly excited and enhanced by incident light at θ_C, whereas the near-field signal on the cell surface reaches a maximum at θ_{SP}. Therefore, the subcellular regions, in which the fluorophores are located, can be resolved by the angular distribution curves. Images in different excitation modes also demonstrate the capability of VANFM for subcellular detection.

VANFM Imaging for EGFR-Mediated Endocytosis. The axial distance-dependent coupling of fluorophores with surface plasmons enables VANFM to efficiently detect biological activities in different subcellular regions in the axial dimension simply by varying the incident angles. With the high-resolution optical-sectioning capability of our system, the dynamics of receptor-mediated endocytosis in Caski cells can be determined. Epidermal growth factor (EGF) receptor (EGFR) endocytosis, which is behind the biological response of the EGF-activated signaling pathway, is essential for the activities of normal cells as well as cancer cells.[54−58] To follow the fate of EGFR and its ligand EGF over time, we incubated cells with Alexa Fluor 555 conjugated to EGF (AF 555-EGF; Molecular Probes). Cells were then imaged with VANFM after internalization for different periods of time (0, 5, 10, and 30 min, respectively). Further details of the sample preparation can be found in the Experimental Section.

The angular distributions and fluorescence images revealed the movements of ligand–receptor complexes over time (Figure 3). The relative intensities of the two peaks in the angular distribution curves changed as the endocytic time increased. For cells that were fixed immediately after the incubation at 4 °C, the complexes simply rested on the membrane due to the low endocytic activity. Since the fluorophores were in the close vicinity of the Au substrate within the coupling region, the strongest near-field fluorescence can be obtained by θ_{SP} excitation (Figure 3a). As ligand–receptor complexes were internalized, the signal of far-field components (I_C) intensified while that of near-field components (I_{SP}) weakened (Figure 3b and Figure 3c). Ultimately, I_{SP} faded away while I_C was maximized, which means that most of the complexes were internalized into the

DOI: 10.1021/acs.analchem.9b02845
Anal. Chem. 2019, 91, 13658−13664

cytoplasm. As the results show, the angular distributions can reflect the axial distributions of the complexes in subcellular regions. For comparison, we did control experiments on uncoated coverslips. There was only one angular peak at θ_C throughout the endocytosis process with TIRFM (Figure S7). Moreover, variation of the imaging depth with different incident angles provides a method to observe the different aggregation levels of ligand−receptor complexes. For this reason, we could trace cargo depth by capturing images at different angles.

To further investigate the axial distributions of EGF-EGFR complexes during endocytosis, we analyzed the relative ratio (ρ) of the near-field component signal (I_{SP}) to the far-field component signal (I_C; $\rho = I_{SP}/I_C$; Figure 4). As indicated by the histogram, the ρ decreased with time, resulting from the axial migration of ligand−receptor complexes. Before endocytosis, the complexes were resting on the plasm membrane. Thus, fluorophores were mainly distributed within coupling region, resulting in the largest value of ρ. As the complexes progressively internalize, the intensity of the near-field fluorophores decreased while that of the far-field components increased so that ρ diminished rapidly. After approximately 10 min, the value of ρ stabilized, indicating that most complexes had been internalized into the cytoplasm. The relative I_{SP}/I_C ratio can provide a semiquantitative estimate of the axial migration of the ligand−receptor complexes in the cell. The smaller the ratio, the smaller the number of molecules on the cell membrane. However, the ratio obtained with TIRFM changed a little during this process (Figure S8). The endocytosis of living cells was then studied with VANFM (section 7, Supporting Information). Similarly, the value of ρ decreased as endocytosis took place. However, a slower decrease of ρ was obtained due to the lower endocytic activity at room temperature (Figure S9 (b)). This phenomenon demonstrates the high sensitivity and axial-resolution of VANFM for tracking endocytosis in cells. Meanwhile, as this estimate requires the recording of only two images, our approach could significantly shorten the experimental time, which is a definite advantage for living cell observation. Moreover, tracing the endocytic pathway with intensity ratios could effectively reduce the interference of the excitation intensity and fluorophore concentration, which seriously hinder conventional intensity-based detection.

CONCLUSIONS

We report the development of an axially resolved VANFM with potential applications in cellular imaging. This imaging technique, utilizing a semitransparent Au substrate to realize both surface plasmon resonance excitation and critical angle excitation, expands the imaging range from the cell membrane to deep subcellular regions with ultrahigh axial resolution for the membrane. The relationship between the angular distribution and molecule−substrate distance provides a method to localize the fluorophores. Imaging of membrane-stained and nucleus-stained cells displayed different angle distributions in VANFM because of the distribution of the fluorophores in the axial direction. Such a distribution cannot be demonstrated using conventional TIRFM. This method also allows the recording of subcellular images with high axial resolution by exciting samples with suitable illumination angles through variation of the penetration depth of the evanescent wave. With critical angle excitation, molecules located in cytoplasm and nucleus could be recorded. With SPR excitation, only the events near the cell membrane can be observed, resulting from the confined axial-section with the thickness of around 50 nm. In the study of EGFR-mediated endocytosis, the angular distribution curves and intensity ratios showed an evolution of the signal, which revealed the axial migration of ligand−receptor complexes over time. In addition, the angular distribution curves and relative intensity ratios at different incident angles, used to localize the molecules in axial direction, could effectively overcome the interference of the fluctuations in the excitation intensity and fluorophore concentration as well as individual differences among cells.

In conclusion, VANFM provides a novel approach to localize the molecular distribution in the axial dimension with better axial resolution than TIRFM. The setup is built on top of a conventional TIRFM simply with the addition of a half wave plate and Au-coated coverslip, thus allowing its application in a broader range of studies. In this report, we have focused on the application of VANFM in investigating EGFR-mediated endocytosis, which shows high axial resolution. However, we suggest that the potential of this technique for life-science applications is much wider, especially with regard to the membrane-related cellular activities, such as cell proliferation, adhesion, and migration.

ASSOCIATED CONTENT

Supporting Information

The Supporting Information is available free of charge on the ACS Publications website at DOI: 10.1021/acs.analchem.9b02845.

Experimental procedures and supporting figures (PDF)

AUTHOR INFORMATION

Corresponding Author

*E-mail: yaoqunli@xmu.edu.cn.

ORCID

Yao-Qun Li: 0000-0001-7842-1671

Author Contributions

All authors have given approval to the final version of the manuscript.

Notes

The authors declare no competing financial interest.

ACKNOWLEDGMENTS

Financial support from the National Natural Science Foundation of China (21874110, 21375111, 21505109, and 21521004), the 973 Program of China (2013CB933703), and the Fund of the Ministry of Education of China (PCSIRT IRT17R66) is gratefully acknowledged. We thank Professor Richard N. Zare and Professor Bruno Robert for their critical reading of this manuscript.

REFERENCES

(1) Conner, S. D.; Schmid, S. L. *Nature* **2003**, *422* (6927), 37−44.

(2) Wu, L. G.; Hamid, E.; Shin, W.; Chiang, H. C. *Annu. Rev. Physiol.* **2014**, *76*, 301−331.

(3) Barbieri, E.; Di Fiore, P. P.; Sigismund, S. *Curr. Opin. Cell Biol.* **2016**, *39*, 21−27.

(4) Renard, H. F.; Simunovic, M.; Lemiere, J.; Boucrot, E.; Garcia-Castillo, M. D.; Arumugam, S.; Chambon, V.; Lamaze, C.; Wunder, C.; Kenworthy, A. K.; Schmidt, A. A.; McMahon, H. T.; Sykes, C.; Bassereau, P.; Johannes, L. *Nature* **2015**, *517* (7535), 493−496.

DOI: 10.1021/acs.analchem.9b02845
Anal. Chem. 2019, 91, 13658−13664

(5) Sun, E.-Z.; Liu, A.-A.; Zhang, Z.-L.; Liu, S.-L.; Tian, Z.-Q.; Pang, D.-W. *ACS Nano* **2017**, *11* (5), 4395−4406.
(6) Wu, X.; Liu, H.; Liu, J.; Haley, K. N.; Treadway, J. A.; Larson, J. P.; Ge, N.; Peale, F.; Bruchez, M. P. *Nat. Biotechnol.* **2003**, *21* (1), 41−46.
(7) Pena, B.; Barhoumi, R.; Burghardt, R. C.; Turro, C.; Dunbar, K. R. *J. Am. Chem. Soc.* **2014**, *136* (22), 7861−7864.
(8) Wang, S.; Kong, H.; Gong, X.; Zhang, S.; Zhang, X. *Anal. Chem.* **2014**, *86* (16), 8261−8266.
(9) Betzig, E.; Patterson, G. H.; Sougrat, R.; Lindwasser, O. W.; Olenych, S.; Bonifacino, J. S.; Davidson, M. W.; Lippincott-Schwartz, J.; Hess, H. F. *Science* **2006**, *313* (5793), 1642−1645.
(10) Lichtman, J. W.; Conchello, J. A. *Nat. Methods* **2005**, *2* (12), 910−919.
(11) Huang, B.; Bates, M.; Zhuang, X. *Annu. Rev. Biochem.* **2009**, *78*, 993−1016.
(12) Hein, B.; Willig, K. I.; Hell, S. W. *Proc. Natl. Acad. Sci. U. S. A.* **2008**, *105* (38), 14271−14276.
(13) Archetti, A.; Glushkov, E.; Sieben, C.; Stroganov, A.; Radenovic, A.; Manley, S. *Nat. Commun.* **2019**, *10* (1), 1267.
(14) Huang, B.; Bates, M.; Zhuang, X. *Annu. Rev. Biochem.* **2009**, *78*, 993−1016.
(15) Liu, W.; Toussaint, K. C.; Okoro, C.; Zhu, D.; Chen, Y.; Kuang, C.; Liu, X. *Laser Photonics Rev.* **2018**, *12* (8), 1700333.
(16) Sako, Y.; Minoguchi, S.; Yanagida, T. *Nat. Cell Biol.* **2000**, *2* (3), 168−172.
(17) Allersma, M. W.; Wang, L.; Axelrod, D.; Holz, R. W. *Mol. Biol. Cell* **2004**, *15* (10), 4658−4668.
(18) Trexler, A. J.; Sochacki, K. A.; Taraska, J. W. *Mol. Biol. Cell* **2016**, *27* (15), 2423−2434.
(19) Mattheyses, A. L.; Simon, S. M.; Rappoport, J. Z. *J. Cell Sci.* **2010**, *123* (21), 3621−3628.
(20) Boulanger, J.; Gueudry, C.; Münch, D.; Cinquin, B.; Paul-Gilloteaux, P.; Bardin, S.; Guérin, C.; Senger, F.; Blanchoin, L.; Salamero, J. *Proc. Natl. Acad. Sci. U. S. A.* **2014**, *111* (48), 17164−17169.
(21) Mattheyses, A. L.; Axelrod, D. *J. Biomed. Opt.* **2006**, *11* (1), 014006.
(22) Konopka, C. A.; Bednarek, S. Y. *Plant J.* **2008**, *53* (1), 186−196.
(23) Luo, W.; Xia, T.; Xu, L.; Chen, Y. G.; Fang, X. *J. Biophotonics* **2014**, *7* (10), 788−798.
(24) Zhang, K.; Osakada, Y.; Vrljic, M.; Chen, L.; Mudrakola, H. V.; Cui, B. *Lab Chip* **2010**, *10* (19), 2566−2573.
(25) Tokunaga, M.; Imamoto, N.; Sakata-Sogawa, K. *Nat. Methods* **2008**, *5*, 159−161.
(26) Gryczynski, Z.; Borejdo, J.; Calander, N.; Matveeva, E. G.; Gryczynski, I. *Anal. Biochem.* **2006**, *356* (1), 125−131.
(27) Tang, W. T.; Chung, E.; Kim, Y.; So, P. T. C.; Sheppard, C. J. R. *Appl. Phys. A: Mater. Sci. Process.* **2007**, *89* (2), 333−335.
(28) Ge, B.; Ma, Y.; Kuang, C.; Zhang, D.; Toussaint, K. C., Jr.; You, S.; Liu, X. *Opt. Express* **2015**, *23* (10), 13159−13171.
(29) Borejdo, J.; Gryczynski, Z.; Fudala, R.; Joshi, C. R.; Borgmann, K.; Ghorpade, A.; Gryczynski, I. *J. Biomed. Opt.* **2018**, *23* (06), 1.
(30) Mettikolla, P.; Calander, N.; Luchowski, R.; Gryczynski, I.; Gryczynski, Z.; Borejdo, J. *J. Biomed. Opt.* **2010**, *15* (1), 017011.
(31) Yuk, J. S.; McDonagh, C.; MacCraith, B. D. *Anal. Bioanal. Chem.* **2010**, *398* (5), 1947−1954.
(32) Burghardt, T. P.; Charlesworth, J. E.; Halstead, M. F.; Tarara, J. E.; Ajtai, K. *Biophys. J.* **2006**, *90* (12), 4662−4671.
(33) Yuk, J. S.; MacCraith, B. D.; McDonagh, C. *Biosens. Bioelectron.* **2011**, *26* (7), 3213−3218.
(34) He, R.-Y.; Lin, C.-Y.; Su, Y.-D.; Chiu, K.-C.; Chang, N.-S.; Wu, H.-L.; Chen, S.-J. *Opt. Express* **2010**, *18* (4), 3649−3659.
(35) Schreiber, B.; Heil, H. S.; Kamp, M.; Heinze, K. G. *Opt. Express* **2018**, *26* (16), 21301−21313.
(36) Borejdo, J.; Calander, N.; Gryczynski, Z.; Gryczynski, I. *Opt. Express* **2006**, *14* (17), 7878−7888.
(37) Calander, N.; Muthu, P.; Gryczynski, Z.; Gryczynski, I.; Borejdo, J. *Opt. Express* **2008**, *16* (17), 13381−13390.
(38) Mettikolla, P.; Calander, N.; Luchowski, R.; Gryczynski, I.; Gryczynski, Z.; Borejdo, J. *J. Biomed. Opt.* **2010**, *15* (1), 017011.
(39) Fu, Y.; Winter, P. W.; Rojas, R.; Wang, V.; McAuliffe, M.; Patterson, G. H. *Proc. Natl. Acad. Sci. U. S. A.* **2016**, *113* (16), 4368−4373.
(40) Zhu, J.; Liao, L.; Zhu, L.; Zhang, P.; Guo, K.; Kong, J.; Ji, C.; Liu, B. *Talanta* **2013**, *107*, 408−415.
(41) Axelrod, D. *Traffic* **2001**, *2* (11), 764−774.
(42) Lakowicz, J. R. *Anal. Biochem.* **2004**, *324* (2), 153−169.
(43) Malicka, J.; Gryczynski, I.; Gryczynski, Z.; Lakowicz, J. R. *Anal. Chem.* **2003**, *75* (23), 6629−6633.
(44) Cao, S. H.; Cai, W. P.; Liu, Q.; Xie, K. X.; Weng, Y. H.; Huo, S. X.; Tian, Z. Q.; Li, Y. Q. *J. Am. Chem. Soc.* **2014**, *136* (19), 6802−6805.
(45) Srinivasan, V.; Vernekar, D.; Jaiswal, G.; Jagadeesan, D.; Ramamurthy, S. S. *ACS Appl. Mater. Interfaces* **2016**, *8* (19), 12324−12329.
(46) Aslan, K.; Geddes, C. D. *Anal. Chem.* **2009**, *81* (16), 6913−6922.
(47) Cao, S. H.; Zou, Z. X.; Weng, Y. H.; Cai, W. P.; Liu, Q.; Li, Y. Q. *Biosens. Bioelectron.* **2014**, *58*, 258−265.
(48) Cao, S. H.; Xie, T. T.; Cai, W. P.; Liu, Q.; Li, Y. Q. *J. Am. Chem. Soc.* **2011**, *133* (6), 1787−1789.
(49) Zhang, D. G.; Moh, K. J.; Yuan, X. C. *Opt. Express* **2010**, *18* (12), 12185−12190.
(50) Gryczynski, I.; Malicka, J.; Nowaczyk, K.; Gryczynski, Z.; Lakowicz, J. R. *J. Phys. Chem. B* **2004**, *108* (32), 12073−12083.
(51) Campagnola, P. J.; Balaa, K.; Stelzer, E. H. K.; Devauges, V.; Goulam, Y.; von Bally, G.; Studer, V.; Lévêque-Fort, S.; Fort, E. *Proc. SPIE* **2009**, *7367*, 736710.
(52) Liu, Q.; Cao, S. H.; Cai, W. P.; Liu, X. Q.; Weng, Y. H.; Xie, K. X.; Huo, S. X.; Li, Y. Q. *J. Phys. Chem. B* **2015**, *119* (7), 2921−2927.
(53) Xie, K. X.; Cao, S. H.; Wang, Z. C.; Weng, Y. H.; Huo, S. X.; Zhai, Y. Y.; Chen, M.; Pan, X. H.; Li, Y. Q. *Sens. Actuators, B* **2017**, *253*, 804−808.
(54) Yewale, C.; Baradia, D.; Vhora, I.; Patil, S.; Misra, A. *Biomaterials* **2013**, *34* (34), 8690−8707.
(55) Tomas, A.; Futter, C. E.; Eden, E. R. *Trends Cell Biol.* **2014**, *24* (1), 26−34.
(56) Tan, X.; Lambert, P. F.; Rapraeger, A. C.; Anderson, R. A. *Trends Cell Biol.* **2016**, *26* (5), 352−366.
(57) Li, H.; You, L.; Xie, J.; Pan, H.; Han, W. *Cell. Signalling* **2017**, *35*, 223−230.
(58) Tan, X.; Thapa, N.; Sun, Y.; Anderson, R. A. *Cell* **2015**, *160* (1−2), 145−160.

DOI: 10.1021/acs.analchem.9b02845
Anal. Chem. 2019, 91, 13658−13664